nature nanotechnology

ARTICLES

https://doi.org/10.1038/s41565-019-0584-x

A high-performance topological bulk laser based on band-inversion-induced reflection

Zeng-Kai Shao[1,2,3,6], Hua-Zhou Chen[1,2,3,6], Suo Wang[1,2,3,6], Xin-Rui Mao[1,2,3], Zhen-Qian Yang[1,2,3], Shao-Lei Wang[1], Xing-Xiang Wang[4,5], Xiao Hu[4,5] and Ren-Min Ma[1,2,3]*

Topological insulators are materials that behave as insulators in the bulk and as conductors at the edge or surface due to the particular configuration of their bulk band dispersion. However, up to date possible practical applications of this band topology on materials' bulk properties have remained abstract. Here, we propose and experimentally demonstrate a topological bulk laser. We pattern semiconductor nanodisk arrays to form a photonic crystal cavity showing topological band inversion between its interior and cladding area. In-plane light waves are reflected at topological edges forming an effective cavity feedback for lasing. This band-inversion-induced reflection mechanism induces single-mode lasing with directional vertical emission. Our topological bulk laser works at room temperature and reaches the practical requirements in terms of cavity size, threshold, linewidth, side-mode suppression ratio and directionality for most practical applications according to Institute of Electrical and Electronics Engineers and other industry standards. We believe this bulk topological effect will have applications in near-field spectroscopy, solid-state lighting, free-space optical sensing and communication.

Topological insulators have become the focus of substantial research efforts in recent years owing to their novel edge/interface states protected by the topological property of the bulk band dispersion, a notion known as the bulk–edge correspondence[1–3]. In 2008, Haldane and Raghu developed the concept of band topology to the realm of photonics[4,5]. Subsequently, the bulk–edge correspondence has been explored as a new knob for manipulating light for various optical designs. Photonic analogues of quantum Hall effect[6–8], quantum spin Hall effect[9–13], topological crystalline insulator[14–18], quantum valley Hall effect[19], three-dimensional topological insulator[20–22] and other topological states of electrons[23–27] were proposed and partially demonstrated in experiments. Most recently, photonic topology has been employed in laser physics and devices aiming at achieving stable lasing based on the topologically protected edge states. Until now, topological lasers, such as coupled sites based on the one-dimensional Su–Schrieffer–Heeger model[28–30], magneto-optic photonic crystals in the presence of a magnetic field[31] and topological insulator lasers based on coupled ring-resonator array[32,33] have been developed, giving rise to improved performance compared to their trivial counterparts. All these efforts have contributed to launch a new field called topological photonics, where photonic topology is exploited to harness light, and have already overturned some of the traditional views on electromagnetic wave propagation and manipulation[27]. However, so far, the possible impact of band topology on bulk properties has acquired much less attention and its potential applications are yet to be explored.

Here, we report on a topological bulk lasing phenomenon based on an architected nanocavity array. In the present laser cavity, a bulk state of a topological photonic crystal around the band edge at the Γ point is laterally confined by a trivial photonic crystal since it acquires opposite parity due to the band inversion. The band-inversion-induced confinement occurs in a small range of wave vectors around the Γ point that provides a novel lasing mode selection mechanism and renders emission directionality. These properties are distinct from topological lasers based on edge/interface states reported so far[28–32] and we therefore call the present device a topological bulk laser. The experimentally demonstrated topological bulk laser operates at room temperature in a single mode with a side-mode suppression ratio over 36 dB, which remarkably reaches the requirement for most practical applications including telecommunication, laser printing and sensing according to Institute of Electrical and Electronics Engineers and other industry standards[34,35]. The threshold of the topological bulk laser is of the order of kW cm^{-2}, which is comparable to those found in commercial laser diodes[35]. We further show that the topological bulk laser emits vertically with divergence angles less than 6°, despite its microscale cavity size. Key metrics including cavity size, operation temperature, threshold, linewidth, side-mode suppression ratio and directionality of the topological bulk laser and other representative small lasers are shown in Supplementary Part 1, which verifies the high performance of the present device. The reflection mechanism demonstrated here leads to applications of topological devices beyond edge/interface effects, and can also be applicable for other wave-related fields including electronics, acoustics and phononics.

Basic principle to construct a topological bulk laser

Figure 1 shows the basic principle of the topological bulk laser where nanocavity arrays with bulk bands distinct in topology are architected from a single nanocavity step by step. First, we begin with a semiconductor nanodisk cavity and focus on its dipole and quadrupole modes, which carry different frequencies (Fig. 1a). Second, individual nanocavities are arranged in a triangular lattice where dipole and quadrupole bands will be formed (left panel of Fig. 1b). Third, six triangle nanoholes are introduced into each nanocavity to fine tune the frequency of dipole and quadrupole

[1]State Key Lab for Mesoscopic Physics and School of Physics, Peking University, Beijing, China. [2]Collaborative Innovation Center of Quantum Matter, Beijing, China. [3]Frontiers Science Center for Nano-optoelectronics, Peking University, Beijing, China. [4]International Center for Materials Nanarchitectonics, National Institute for Materials Science, Tsukuba, Japan. [5]Graduate school of Pure and Applied Sciences, University of Tsukuba, Tsukuba, Japan. [6]These authors contributed equally: Zeng-Kai Shao, Hua-Zhou Chen, Suo Wang. *e-mail: renminma@pku.edu.cn

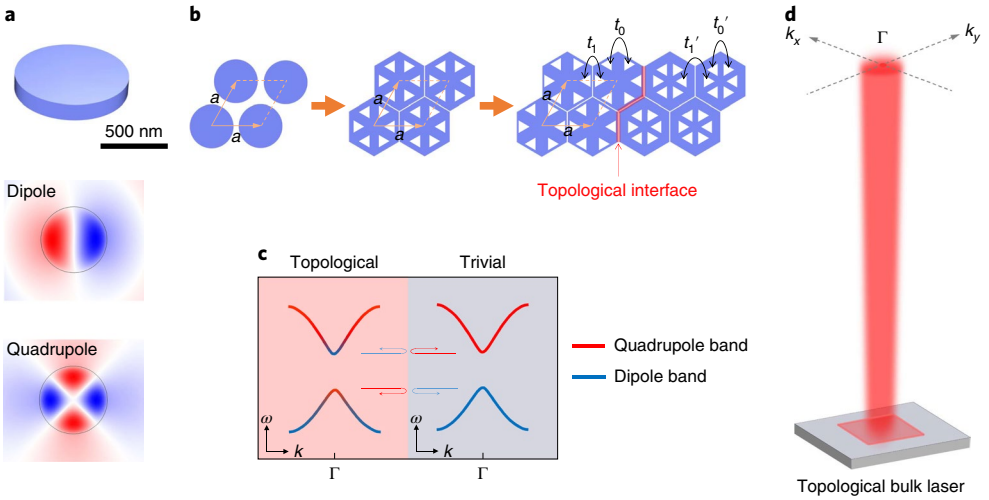

Fig. 1 | Principle of the construction of the topological bulk laser. a, Schematic of a single semiconductor nanodisk cavity employed to construct a topological bulk laser (top panel). Its dipole and quadrupole modes with opposite parities (bottom two panels) are used to achieve band inversion in a topological state. Blue and red colours indicate opposite phases. (The scale bar only applies to the top panel.) **b**, Left, arranging nanocavities into a triangular lattice to form dipole and quadrupole energy bands. Middle, six triangle nanoholes are introduced into each shape-transformed nanocavity to fine tune the dipole and quadrupole bands. Right, the triangle nanoholes are moved away from or towards the individual centres of nanocavities to form topological and trivial photonic energy bands, respectively. a denotes the lattice constant. t_0 and t_0' denote the strengths of intracell coupling. t_1 and t_1' denote the strengths of intercell coupling. **c**, Schematic band diagram when topological and trivial photonic crystals are put in contact in real-space. Because of the band inversion at the Γ point, at a frequency around the band edges the bulk modes in the topological and trivial regions possess opposite parities, leading to the band-inversion-induced reflection (indicated by the arrows). Note that the bands in the topological and trivial regions are doubly degenerate. ω and k denote frequency and wavenumber. **d**, Schematic of a topological bulk laser with in-plane field confinement based on the band-inversion-induced reflection. The in-plane red area indicates the topological cavity. A unique feature of the band-inversion-induced reflection is that it occurs only around the band edge at the Γ point, which endows topological bulk lasers with fine out-of-plane directional emission. k_x and k_y indicate in-plane momenta.

bands with topological features. Note that here the circular nanocavities in the lattice are transformed into a hexagonal shape to avoid uncontrollable band coupling induced by air gaps between nanocavities. When the nanoholes are arranged in a honeycomb lattice, dipole and quadrupole bands of the nanocavity array become degenerate and form Dirac-type photonic dispersion around the Γ point (middle panel of Fig. 1b). Lastly, we move the triangle nanoholes away from or towards the individual centres of hexagonal nanocavities. Consequently, two architected nanocavity arrays distinct in topology are formed due to a band inversion between the dipole and quadrupole bands at the Γ point, as shown in the right panel of Fig. 1b(ref. [14,16]). At the real-space interface between the two photonic crystals distinct in topology, there arises a new reflection mechanism effective for photon states with frequency close to the band edges at the Γ point, since the states in the trivial photonic crystal cannot propagate into the topological photonic crystal, and vice versa, due to the opposite parities of wavefunctions, as shown schematically in Fig. 1c. This band-inversion-induced reflection can be exploited as a new type of feedback mechanism to construct topological bulk lasers, where light waves get reflected at the in-plane enclosed interface forming effective cavity feedback for lasing as shown schematically in Fig. 1d. The notion that a band inversion between two bands with opposite parities can induce a topological state has been established since the birth of the quantum spin Hall effect, as revealed by the Bernevig–Hugues–Zhang model[36], where the band inversion is induced by spin–orbit coupling. Here, in the topological photonic crystal made of dielectric materials, it is the two ways of deformation of the honeycomb structure, both respecting the C_{6v} crystalline symmetry, which renders the band inversion and the photonic analogue of the quantum spin Hall effect[14].

The topological nature of the present laser arises from the laser cavity defined in the topological way, which yields a novel mode selection mechanism and the emission directionality. First, the cavity of the topological bulk laser is defined by the in-plane interface between two photonic crystals distinct in topology (Supplementary Parts 2–4). Second, the band-inversion-induced reflection at the cavity boundaries originates from the construction of a topologically non-trivial photonic crystal from a topologically trivial one. In the present dielectric honeycomb-type photonic crystal, the band inversion between the p band and d band of opposite parities at the Γ point is the necessary and sufficient condition for constructing the topologically non-trivial phase (Supplementary Part 2). Moreover, the band-inversion-induced reflection only occurs around the Γ point (Fig. 1c), which provides a novel lasing mode selection mechanism and enables directional lasing emission of cavity modes (Fig. 1d). As is well known, arranging nanolasers into photonic/plasmonic crystals yields a macroscopic response that may be quite different from individual nanolasers[37–41]. Here the judicious eigenmode engineering with control over the eigenmode symmetry and topology leads to a topological bulk laser with unprecedented features. As a common wisdom of topology physics, topological indices give the number of topological edge states, which are not used in the present design.

Topological bulk laser cavity

We employ the deformed honeycomb photonic crystals with topological and trivial band structures to construct our topological bulk laser, where the gain material is indium gallium arsenide phosphide (InGaAsP) multi-quantum wells (MQWs) emitting at telecommunication wavelength. Fig. 2a shows the scanning electron microscopy (SEM) images of our device, where a topological bulk laser is formed by a trivial photonic crystal encircling a topological photonic crystal inside. The common lattice constant of the two photonic crystals, a, is 820 nm. The topological and trivial photonic bands are achieved by changing the ratio between the lattice constant a and the distance R between the centre of the unit cell and

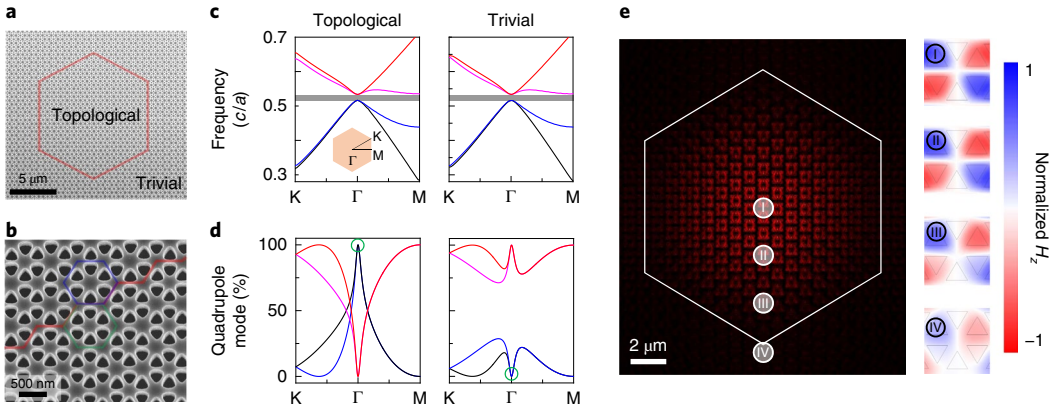

Fig. 2 | Topological bulk laser cavity. a, SEM image of a fabricated topological bulk laser, which is composed of a topological photonic crystal encircled by a trivial photonic crystal. The red hexagon indicates the topological interface. **b**, Enlarged SEM image of structures suspended in air with individual layers of MQWs clearly visible. The red line represents the topological interface, the blue hexagon indicates a unit nanocavity in the topological photonic crystal and the green hexagon indicates a unit nanocavity in the trivial photonic crystal. **c**, Band structures of the topological and trivial photonic crystals obtained from full-wave simulations. The topological and trivial photonic crystals share a common frequency bandgap at the Γ point based on judicious tuning. Grey areas indicate the bandgaps of the photonic crystals. Inset: the first Brillouin zone of the photonic crystals. *c* and α denote the speed of light in vacuum and the lattice constant of photonic crystals, respectively. **d**, The corresponding weight of the quadrupole mode in the four bands obtained from the tight-binding model. Around the Γ point, the two lower frequency bands are in pure quadrupole mode in the topological photonic crystal due to band inversion, whereas the two lower frequency bands in the trivial photonic crystal are in pure dipole mode where the weight of the quadrupole mode approaches 0. Same color in **c** and **d** indicates the same frequency band. **e**, Electric field ($|E|^2$) distribution of a confined cavity mode obtained by full-wave simulations. The operating frequency lies at the band edge below the bandgap (marked by the green circles in **d**). The white hexagon represents the topological interface. The electromagnetic field is well confined within the topological bulk cavity. Right insets are the enlarged out-plane magnetic field distributions (H_z) in four unit cells marked as I, II, III and IV, respectively, which clearly show that all the individual nanocavities carry the quadrupole mode and oscillate in phase inside the cavity.

the centre of each triangle nanohole (side length ~ 260 nm) inside a hexagonal unit cell[14,16]. The side length of the hexagonal topological bulk laser cavity is 7.38 μm. The quantum wells can be seen clearly in the etched nanoholes as bright and dark layers in the enlarged SEM image in Fig. 2b. The structure was fabricated by electron-beam lithography followed by dry etching to define the nanoholes. Subsequently, the indium phosphide (InP) substrate was removed by wet etching with hydrochloric acid, ending with the suspended membrane (see Methods and Supplementary Part 5). The devices were optically pumped with pulsed lasers at room temperature (see Methods). The optical characterization setup is discussed in the Methods and shown in Supplementary Part 6.

In the following, we briefly illustrate the origin of the band inversion and non-trivial topology in terms of the tight-binding model of the honeycomb lattice. Taking a hexagonal unit cell, which includes six sites, the effective Hamiltonian is given by[14,16,42]

$$H = H_0 + H_1 = -t_0 \sum\nolimits_{\langle i,j\rangle} a_i^\dagger a_j - t_1 \sum\nolimits_{\langle i',j'\rangle} a_{i'}^\dagger a_{j'} \qquad (1)$$

where a_i ($a_i^\dagger$) is the annihilation (creation) operator at site i, and t_0 and t_1 are the coupling strengths between nearest-neighbour sites inside and between hexagonal unit cells. The six eigenvectors of H_0 for a single unit cell are $|s\rangle$, $|p_x\rangle$, $|p_y\rangle$, $|d_{x^2-y^2}\rangle$, $|d_{xy}\rangle$ and $|f\rangle$, and the corresponding eigenenergies are $-2t_0$,$-t_0$,$-t_0$,t_0,t_0 and $2t_0$, respectively (Supplementary Part 3). *s* and *f* denote monopole and hexapole modes respectively. In a single hexagonal unit cell, quadrupole (*d*) modes possess a higher energy (t_0) than dipole (*p*) modes ($-t_0$). In the presence of intercell coupling, the energy of dipole modes (quadrupole modes) increases (decreases) by t_1 at the Γ point for a bulk system, which leads to a *p*–*d* band inversion and non-trivial topology at $t_1 > t_0$ (Fig. 1b and Supplementary Part 3).

To exclude the conventional bandgap reflection-induced feedback, an identical bandgap is designed for the trivial and topological photonic crystals. The bandgap between the quadrupole band and dipole band at the Γ point is $2|t_1 - t_0|$. In the normal honeycomb lattice, the distances between individual sites are identical, and thus the intra- and intercell coupling strengths are equal. In this case, the quadrupole and dipole modes are degenerate, forming Dirac cones at the Γ point with linear dispersion relation. By shrinking or expanding the positions of the six holes within the unit cell, the bandgap for the trivial state and the bandgap for the topological state can be judiciously tuned to be the same. In our design, $R_1 = 0.95 \times (a/3)$ (shrunken) for the trivial photonic crystal and $R_2 = 1.04 \times (a/3)$ (expanded) for the topological photonic crystal. The dispersion curves of the trivial and topological photonic crystals are shown in Fig. 2c, where the two bandgaps share the same size and position. The corresponding quadrupole mode weights of these four modes obtained from the tight-binding model are shown in Fig. 2d. In the topological case, the upper (lower) two frequency bands transform to dipole modes (quadrupole modes), while in the trivial case, the upper (lower) two frequency bands are quadrupole modes (dipole modes) at the Γ point, constituting the band inversion. The band inversion and the identical bandgap in the trivial and topological photonic crystals ensure the reflection induced by the mismatch of wavefunction parity and exclude the reflection from the conventional bandgap effect in photonic crystals.

Fig. 2e shows the full-wave simulated fundamental cavity mode at the low-frequency side of the bandgap (marked by green circles in Fig. 2d) where the electromagnetic field is well confined in the topological bulk laser cavity (see Methods). In the cavity, all the individual nanocavities oscillate in phase, and hence the cavity mode can be assigned as $l = 0$ referring to the global orbital angular momentum with respect to the device centre (Supplementary Part 4). The enlarged pictures of regions I, II, III and IV are shown in the insets of Fig. 2e, where we observe that all the individual nanocavities oscillate in quadrupole mode and in phase inside the cavity. Compared to the dipole mode in the energy band, the quadrupole

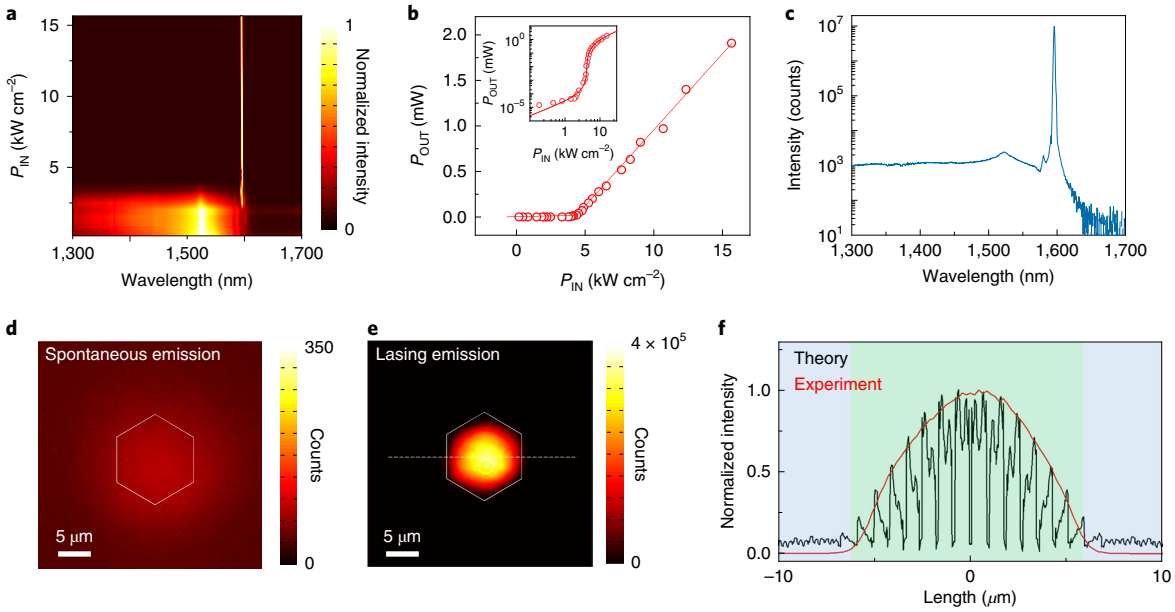

Fig. 3 | Lasing characteristics of topological bulk laser. a, Normalized emission spectra at various pump powers. When pumped above the lasing threshold, a single-mode lasing occurs in the topological cavity. **b**, Integrated output power as a function of pump intensity on a linear scale. Inset: curve on a log scale. Circles represent the data and curves represent the fitting. The lasing threshold is as small as ~4.5 kW cm^{-2}. **c**, Lasing spectrum on a semi-log scale at $2P_{th}$. The side-mode suppression ratio of the topological bulk laser is over 36 dB. **d**, Spontaneous emission pattern. **e**, Lasing emission pattern. In **d** and **e**, white hexagons indicate the cavity interfaces. **f**, Intensity distribution (red curve) along the white dashed line in **e** as compared to the simulated intensity distribution (black curve). The green and blue areas indicate the topological and trivial photonic crystal regions, respectively.

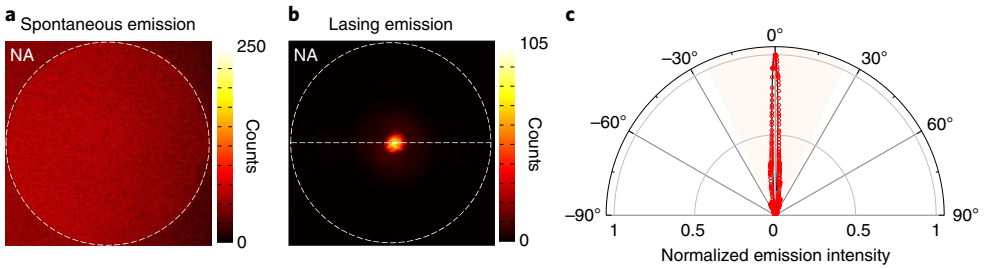

Fig. 4 | Directional emission of the topological bulk laser. a, Angle-resolved far-field pattern of spontaneous emission. **b**, Angle-resolved far-field pattern of lasing emission. In **a** and **b**, dashed circles indicate the numerical aperture (NA = 0.42) of the collection objective. **c**, Red circles represent the angle-resolved intensity profile along the white dashed line in **b**. The full width at half maximum of the emission beam is 5.9°. The black line represents the angle-resolved intensity profile obtained by Fourier transformation from the lasing intensity profile shown in Fig. 3f. The topological bulk laser exhibits high emission directionality, owing to the unique feature of the present design that the band-inversion-induced reflection occurs only around the Γ point. The orange sector area indicates the collection angle of the objective.

mode employed there is a dark mode that enables a high quality factor for the cavity mode[43]. On approaching the topological interface, the field pattern within a unit nanocavity exhibits weaker quadrupole mode characteristics and transforms to the dipole mode outside of the cavity, with the total amplitude suppressed dramatically.

Lasing characteristics of the topological bulk laser

Fig. 3a shows the normalized emission spectra at various pump powers. When pumped above the lasing threshold (P_{th}), a single-mode lasing occurs in the topological cavity. Fig. 3b shows the integrated output power as a function of pump intensity on linear and log scales, indicating a clear transition from the spontaneous emission to the stimulated emission by the kink in the linear scaled curve and the 'S' shape of the log-scaled curve. The measured lasing threshold is as low as ~4.5 kW cm^{-2}, which is comparable to the thresholds of commercial laser diodes.

Fig. 3c shows the lasing spectrum on a semi-log scale at $2P_{th}$. The side-mode suppression ratio of the topological bulk laser is over 36 dB. We further use a spectrometer with high spectral resolution to characterize the lasing linewidth, which gives a full width at half maximum of 0.25 nm. This narrow linewidth is comparable to state-of-the-art diode lasers with similar cavity sizes, such as vertical-cavity surface-emitting lasers (Supplementary Parts 1 and 7). The high-performance single-mode lasing of the topological bulk laser originates from the fact that the band-inversion-induced reflection works only around the Γ point where the band inversion takes place. Such a topology-induced mode selection mechanism not only limits the number of cavity modes with efficient confinement, but also gives the mode closer to the band edge a higher quality factor (Supplementary Parts 1 and 8).

The transition between the spontaneous and the stimulated emissions is also observed in real-space emission patterns. When

pumped below threshold, the emission pattern is uniform over the gain region as shown in Fig. 3d. However, the emission above the lasing threshold shows a well-defined pattern as shown in Fig. 3e. We have confirmed that the lasing mode is the fundamental mode of the topological cavity with $l=0$ by comparing the lasing pattern with the numerically simulated one shown in Fig. 2e. In Fig. 3f, the line field distributions are extracted from experimental and calculated patterns for comparison, and their profiles match well with each other.

Notably, the topological lasing takes place at the frequency where there are photon states both inside and outside the cavity, which is in stark contrast with the conventional feedback induced by photonic bandgap and dielectric cladding. In the photonic bandgap cladding case, there is no photon state in the bandgap, whereas in the dielectric cladding case, the cladding layer is a passive material at laser operation frequency. The topological bulk laser is also distinct from the bound state in the continuum lasers[44]. These latter lasers describe waves that remain localized when they coexist with a continuous spectrum of radiating waves[45]. This is clearly not the case for our present device, since the band-inversion-induced confinement takes place in the plane of the photonic crystal structure, which can be a closed system without continuum spectrum.

We note that a dielectric cavity laser of a similar size to our device will host a number of lasing modes[37]. To show this explicitly, we fabricated a dielectric disk laser with the same cavity size as the topological bulk laser, which shows more than ten modes lasing simultaneously (Supplementary Fig. 1). The outputs from multimode lasers are subject to random fluctuations and instabilities because of mode competition, and suffer bad emission directionality. Compared to photonic crystal bandgap-induced confinement, our topological cavity provides more efficient feedback at a given cladding size, since efficient feedback from a photonic crystal bandgap needs fine fabrication and many periodic structures. We confirmed this by replacing the topological photonic crystal with a uniform hexagonal MQW disk, while keeping the trivial photonic crystal unchanged as the cladding. No lasing behaviour was observed at any pump power (Supplementary Fig. 1).

Directional emission of topological bulk laser

The angle-resolved far-field patterns of the laser beam in Fig. 4 show that the topological bulk laser exhibits high emission directionality. At the spontaneous emission region, the laser shows omnidirectional emission indicated by the uniform pattern in momentum space (Fig. 4a). However, when pumped above the lasing threshold, the topological bulk laser emits vertically to the cavity plane with divergence angles less than 6° (Fig. 4b,c). This intensity distribution in momentum space is mainly determined by the microscale lasing spot. The black line in Fig. 4c shows the Fourier-transformed intensity distribution from the real-space lasing intensity profile shown in Fig. 3f, which matches well with the measured angle distribution. The $l=0$ mode is doubly degenerate due to the twofold quadrupole degeneracy. Due to mode competition, the observed single lasing mode is one of the standing wave quadrupole modes with linear polarization (Supplementary Part 9).

Conclusions

In summary, we have demonstrated a topological laser device based on bulk states in a photonic crystal nanocavity array. The mode confinement mechanism stems from the topological transition in which the wavefunctions of bulk states in trivial and topological photonic crystals acquire opposite parities due to the band inversion. Based on this principle, we have constructed a topological bulk laser exhibiting single-mode lasing with vertical emission directionality. We have clarified that the stable single-mode lasing is intimately related to the feedback mechanism with topological origin acting only around the Γ point at the band edges. This effect provides a novel mode selection mechanism. Our work indicates the possibility of exploiting the bulk band structures with non-trivial topology formed by architected nanocavity arrays. This may be useful for collecting topological effects in bulk states beyond the edge and interface effects explored so far. Possible applications lie in near-field spectroscopy, solid-state lighting, free-space optical sensing and communication. The principle is applicable to electronic, acoustic and phononic systems.

Online content

Any methods, additional references, Nature Research reporting summaries, source data, extended data, supplementary information, acknowledgements, peer review information; details of author contributions and competing interests; and statements of data and code availability are available at https://doi.org/10.1038/s41565-019-0584-x.

Received: 13 August 2019; Accepted: 1 November 2019;
Published online: 16 December 2019

References

1. Hasan, M. Z. & Kane, C. L. Colloquium: topological insulators. *Rev. Mod. Phys.* **82**, 3045 (2010).
2. Qi, X. L. & Zhang, S. C. Topological insulators and superconductors. *Rev. Mod. Phys.* **83**, 1057 (2011).
3. Weng, H., Yu, R., Hu, X., Dai, X. & Fang, Z. Quantum anomalous Hall effect and topological electronic states. *Adv. Phys.* **64**, 227–282 (2015).
4. Haldane, F. D. M. & Raghu, S. Possible realization of directional optical waveguides in photonic crystals with broken time-reversal symmetry. *Phys. Rev. Lett.* **100**, 013904 (2008).
5. Raghu, S. & Haldane, F. D. M. Analogs of quantum-Hall-effect edge states in photonic crystals. *Phys. Rev. A* **78**, 033834 (2008).
6. Wang, Z., Chong, Y., Joannopoulos, J. D. & Soljačić, M. Observation of unidirectional backscattering-immune topological electromagnetic states. *Nature* **461**, 772–775 (2009).
7. Rechtsman, M. C. et al. Photonic Floquet topological insulators. *Nature* **496**, 196–200 (2013).
8. Fang, K., Yu, Z. & Fan, S. Microscopic theory of photonic one-way edge mode. *Phys. Rev. B* **84**, 075477 (2011).
9. Khanikaev, A. B. et al. Photonic topological insulators. *Nat. Mater.* **12**, 233–239 (2013).
10. Hafezi, M., Demler, E. A., Lukin, M. D. & Taylor, J. M. Robust optical delay lines via topological protection. *Nat. Phys.* **7**, 907–912 (2011).
11. Hafezi, M., Mittal, S., Fan, J., Migdall, A. & Taylor, J. M. Imaging topological edge states in silicon photonics. *Nat. Photonics* **7**, 1001–1005 (2013).
12. Liang, G. Q. & Chong, Y. D. Optical resonator analog of a two-dimensional topological insulator. *Phys. Rev. Lett.* **110**, 203904 (2013).
13. Ma, T., Khanikaev, A. B., Mousavi, S. H. & Shvets, G. Guiding Electromagnetic waves around sharp corners: topologically protected photonic transport in metawaveguides. *Phys. Rev. Lett.* **114**, 127401 (2015).
14. Wu, L. H. & Hu, X. Scheme for achieving a topological photonic crystal by using dielectric material. *Phys. Rev. Lett.* **114**, 223901 (2015).
15. Barik, S. et al. A topological quantum optics interface. *Science* **359**, 666–668 (2018).
16. Barik, S., Miyake, H., DeGottardi, W., Waks, E. & Hafezi, M. Two-dimensionally confined topological edge states in photonic crystals. *New J. Phys.* **18**, 113013 (2016).
17. Siroki, G., Huidobro, P. A. & Giannini, V. Topological photonics: from crystals to particles. *Phys. Rev. B* **96**, 041408 (2017).
18. Yang, Y. et al. Visualization of a unidirectional electromagnetic waveguide using topological photonic crystals made of dielectric materials. *Phys. Rev. Lett.* **120**, 217401 (2018).
19. Shalaev, M. I., Walasik, W., Tsukernik, A., Xu, Y. & Litchinitser, N. M. Robust topologically protected transport in photonic crystals at telecommunication wavelengths. *Nat. Nanotechnol.* **14**, 31–34 (2019).
20. Slobozhanyuk, A. et al. Three-dimensional all-dielectric photonic topological insulator. *Nat. Photonics* **11**, 130–136 (2016).
21. Yang, Y. et al. Realization of a three-dimensional photonic topological insulator. *Nature* **565**, 622–626 (2019).
22. Lu, L. et al. Symmetry-protected topological photonic crystal in three dimensions. *Nat. Phys.* **12**, 337–340 (2017).

23. Noh, J. et al. Topological protection of photonic mid-gap defect modes. *Nat. Photonics* **12**, 408–415 (2018).
24. Fang, K., Yu, Z. & Fan, S. Realizing effective magnetic field for photons by controlling the phase of dynamic modulation. *Nat. Photonics* **6**, 782–786 (2012).
25. Lu, L., Joannopoulos, J. D. & Soljačić, M. Topological photonics. *Nat. Photonics* **8**, 821–829 (2014).
26. Khanikaev, A. B. & Shvets, G. Two-dimensional topological photonics. *Nat. Photonics* **11**, 763–773 (2017).
27. Ozawa, T. et al. Colloquium: topological photonics. *Rev. Mod. Phys.* **91**, 015006 (2019).
28. St-Jean, P. et al. Lasing in topological edge states of a one-dimensional lattice. *Nat. Photonics* **11**, 651–656 (2017).
29. Parto, M. et al. Edge-mode lasing in 1D topological active arrays. *Phys. Rev. Lett.* **120**, 113901 (2018).
30. Zhao, H. et al. Topological hybrid silicon microlasers. *Nat. Commun.* **9**, 981 (2018).
31. Bahari, B. et al. Nonreciprocal lasing in topological cavities of arbitrary geometries. *Science* **358**, 636–640 (2017).
32. Bandres, M. A. et al. Topological insulator laser: experiments. *Science* **359**, eaar4005 (2018).
33. Harari, G. et al. Topological insulator laser: theory. *Science* **359**, eaar4003 (2018).
34. IEEE Std 802.3 (IEEE, 2015).
35. Michalzik, R. (ed.) VCSELs: fundamentals, technology and applications of vertical-cavity surface-emitting lasers. *Springe. Ser. Optical Sci.* **166**, 560 (2013).
36. Bernevig, B. A., Hughes, T. L. & Zhang, S. C. Quantum spin Hall effect and topological phase transition in HgTe quantum wells. *Science* **314**, 1757–1761 (2006).
37. Ma, R. M. & Oulton, R. F. Applications of nanolasers. *Nat. Nanotechnol.* **14**, 12–22 (2019).
38. Zhou, W. et al. Lasing action in strongly coupled plasmonic nanocavity arrays. *Nat. Nanotechnol.* **8**, 506–511 (2013).
39. Van Beijnum, F. et al. Surface plasmon lasing observed in metal hole arrays. *Phys. Rev. Lett.* **110**, 206802 (2013).
40. Wang, S. et al. Unusual scaling laws for plasmonic lasers beyond diffraction limit. *Nat. Commun.* **8**, 1889 (2017).
41. Ha, S. T. et al. Directional lasing in resonant semiconductor nanoantenna arrays. *Nat. Nanotechnol.* **13**, 1042–1047 (2018).
42. Wu, L. H. & Hu, X. Topological properties of electrons in honeycomb lattice with detuned hopping energy. *Sci. Rep.* **6**, 24347 (2016).
43. Gorlach, M. A. et al. Far-field probing of leaky topological states in all dielectric metasurfaces. *Nat. Commun.* **9**, 909 (2018).
44. Kodigala, A. et al. Lasing action from photonic bound states in continuum. *Nature* **541**, 196–199 (2017).
45. Hsu, C. W., Zhen, B., Stone, A. D., Joannopoulos, J. D. & Soljačić, M. Bound states in the continuum. *Nat. Rev. Mater.* **1**, 16048 (2016).

Methods

Band inversion and non-trivial photonic topology in a honeycomb lattice. A $k\cdot p$ theory can be formulated for the Hamiltonian $H_\Gamma(k)$ describing the band structures near the Γ point presented in Fig. 2b:

$$H_\Gamma(\boldsymbol{k}) = \begin{pmatrix} H_+(\boldsymbol{k}) & 0 \\ 0 & H_-(\boldsymbol{k}) \end{pmatrix},\ H_\pm(\boldsymbol{k}) = \begin{pmatrix} M + B\boldsymbol{k}^2 & Ak_\pm \\ A^* k_\mp & -M - B\boldsymbol{k}^2 \end{pmatrix} \quad (2)$$

where the basis is taken as $[p_+\ d_+\ p_-\ d_-]^{\mathrm{T}}$, which are eigenvectors of orbital angular momentum; $k_\pm = k_x \pm ik_y$, $\boldsymbol{k}^2 = k_x^2 + k_y^2$, are in-plane momenta measured from the Γ point; $B<0$, $M = \omega_p^2 - \omega_d^2$, where M represents effective mass, A is purely imaginary; A and B are given by the hopping energies and lattice constant (Supplementary Part 4); ω_p and ω_d are the eigenfrequencies of the p and d modes at the Γ point. For the honeycomb lattice, $M=0$ corresponding to the Dirac-like photonic dispersion associated with the opposite parties of the p and d orbitals. For the trivial photonic crystals, $M<0$, whereas for the topological photonic crystals, $M>0$, indicating a band inversion in the latter case since $BM<0$. The band inversion between the p and d orbitals in the honeycomb-type lattices gives rise to the non-trivial photonic topology characterized by pseudospin-dependent Chern numbers (Supplementary Part 2). One can also obtain the same topological charges by evaluating directly the Berry curvature and the Berry phase.

Tight-binding model and eigenmodes in a honeycomb lattice. A honeycomb lattice can be viewed as a triangular lattice of hexagonal unit cells with six sites (Supplementary Fig. 4). The Hamiltonian H of the honeycomb lattice includes contributions from couplings inside one unit cell H_0 and those between two unit cells H_1.

$$H = -t_0\Psi^\dagger \begin{pmatrix} 0&1&0&0&0&1\\ 1&0&1&0&0&0\\ 0&1&0&1&0&0\\ 0&0&1&0&1&0\\ 0&0&0&1&0&1\\ 1&0&0&0&1&0 \end{pmatrix} \Psi - t_1\Psi^\dagger \begin{pmatrix} 0&0&0&e^{i\boldsymbol{k}\boldsymbol{a}_1}&0&0\\ 0&0&0&0&e^{i\boldsymbol{k}\boldsymbol{a}_2}&0\\ 0&0&0&0&0&e^{i\boldsymbol{k}(\boldsymbol{a}_2-\boldsymbol{a}_1)}\\ e^{-i\boldsymbol{k}\boldsymbol{a}_1}&0&0&0&0&0\\ 0&e^{-i\boldsymbol{k}\boldsymbol{a}_2}&0&0&0&0\\ 0&0&e^{-i\boldsymbol{k}(\boldsymbol{a}_2-\boldsymbol{a}_1)}&0&0&0 \end{pmatrix} \Psi \quad (3)$$

where t_0 and t_1 describe the intraunit cell and interunit cell coupling strength, respectively. $\mathbf{a}_1$ and $\mathbf{a}_2$ are the primitive lattice vectors (Supplementary Fig. 4b). i is the imaginary unit. The corresponding reciprocal space is shown in Supplementary Fig. 4c. Ψ denotes basic states describing the Wannier functions located at the six different sites inside a unit cell of the hexagonal lattice. The eigenstates of Hamiltonian H_0 are given by $|s\rangle = [1,1,1,1,1,1]^{\mathrm{T}}$, $|p_x\rangle = [1,1,0,-1,-1,0]^{\mathrm{T}}$, $|p_y\rangle = [1,-1,-2,-1,1,2]^{\mathrm{T}}$, $|d_{x^2-y^2}\rangle = [1,1,-2,1,1,-2]^{\mathrm{T}}$, $|d_{xy}\rangle = [1,-1,0,1,-1,0]^{\mathrm{T}}$, $|f\rangle = [1,-1,1,-1,1,-1]^{\mathrm{T}}$, and the corresponding eigenenergies are $-2t_0$,$-t_0$,$-t_0$,t_0,t_0 and $2t_0$, respectively. Note that $|s\rangle$ and $|f\rangle$ are singlets, and construction of pseudospin and pseudo-time-reversal symmetry are valid only for p and d modes, on which we focus here. Using the four eigenstates of the p and d modes of H_0 as the new basis, the Hamiltonian describing the interactions between the p and d modes at the Γ point can be derived (Supplementary Part 3). In the presence of intercell coupling, at the Γ point the eigenenergy of the two p modes shifts to $-t_0+t_1$, while the eigenenergy of the two d modes shifts to $t_0 - t_1$ in a bulk system (Supplementary Figs. 4b and 5).

Cavity modes supported by a topological bulk laser. Starting from the block diagonalized 4×4 Hamiltonian (Supplementary Part 4), we can derive the wavefunctions $\{|1,+\rangle, |2,+\rangle\}$ and eigenenergies E_1 and E_2 for the pseudospin-up sector in a perturbative way where the momentum measured from the Γ point is small. In terms of the new basis $\{|1,+\rangle, |2,+\rangle\}$, we have the following eigenvalue equation:

$$\begin{bmatrix} E_1 & 0 \\ 0 & E_2 \end{bmatrix} \begin{bmatrix} \psi_{1,+} \\ \psi_{2,+} \end{bmatrix} = \lambda \begin{bmatrix} \psi_{1,+} \\ \psi_{2,+} \end{bmatrix} \quad (4)$$

where the eigenvalue λ should be determined by the boundary conditions. Because we are concentrating on the band edge below the bandgap, the second component in the above equation should be picked up and one obtains

$$\nabla^2\psi_{2,+}(r,\phi) + k^2\psi_{2,+}(r,\phi) = 0 \quad (5)$$

where $\psi_{2,+}(r,\phi)$ is the profile wavefunction of the state $|2,+\rangle$ for the unit cell located at r and the azimuthal angle ϕ measured from the centre of the circular cavity, and k is the eigen wavenumber. We are looking for solutions of the above equation with $k^2 \geq 0$, which should exist since the dispersion curve below (above) the bandgap is convex upward (downward) as seen in Fig. 2c. The solution regular at the centre of the system should be

$$\psi_{2,+}(r,\phi) = J_l(kr)e^{il\phi} \quad (6)$$

where $J_l(kr)$ is the Bessel function of the first kind. Due to the mismatch between the parities of wavefunctions in the trivial and topological photonic crystals, the wavefunction inside the cavity should be suppressed to zero at the interface, namely $J_l(kr_c)=0$, where r_c is the radius of the cavity. Therefore, the momentum k and the frequency can only take discrete values given by the zeros of the Bessel functions (see Supplementary Part 4 for more details). In the same way, one can derive the wavefunctions for the pseudospin-down sector.

Device fabrication. We used InGaAsP MQWs grown on InP substrate as gain material, which consists of six 10-nm-thick $In_{x=0.56}Ga_{1-x}As_{y=0.938}P_{1-y}$ well layers sandwiched in 20-nm-thick $In_{x=0.734}Ga_{1-x}As_{y=0.57}P_{1-y}$ barrier layers. Photonic crystals are constructed by etching triangular air holes in the MQWs through electron-beam lithography and chlorine-based inductively coupled plasma etching processes. HCl:H_2O (3:1) was used to etch away InP substrates to form a membrane structure for the laser test (see Supplementary Fig. 9).

Optical characterization. Supplementary Fig. 10 shows our lasing characterization setup. A nanosecond pulse laser (1,064 nm, pulse length 5 ns, repetition rate 12 kHz) was used as the pump source. A long working distance (10 mm) microscope objective (×50) with a numerical aperture of 0.42 was used to focus the pump laser on the topological nanocavities and to collect their emissions using an indium gallium arsenide infrared camera and a near-infrared spectrometer.

Numerical simulation. Optical modes of a topological bulk laser were calculated with the finite-element method based on the commercial software COMSOL Multiphysics. We carried out two-dimensional simulations to calculate the cavity modes, where the effective refractive index of the InGaAsP MQWs was set to be 2.42 and that within the triangle nanoholes was set to be 1. We focused on the optical modes with dominant in-plane electrical field and out-of-plane magnetic field to the semiconductor membrane. The value of the effective refractive index here was determined by matching the frequency of the Dirac point to the system of an effective two-dimensional honeycomb lattice with a finite thickness. The boundary condition in the simulations was set to be a perfect matched layer. In experiments, we used a small spot to pump the bulk laser. To simulate this process, we added an imaginary refractive index ($n_i=-0.03$, estimated from the cavity radiation loss) to the cavity.

Reporting Summary. Further information on research design is available in the Nature Research Reporting Summary linked to this article.

Data availability

The data that support the plots in this paper and other findings of this study are available from the corresponding author on reasonable request.

Acknowledgements

This work is supported by the National Natural Science Foundation of China (grant nos. 11774014, 11574012, 91950115, 61521004), Beijing Natural Science Foundation (grant no. Z180011) and the National Key R&D Program of China (grant no. 2018YFA0704401). X.H. is supported by the CREST Program, Japan Science and Technology Agency (grant no. JPMJCR18T4) and Grants-in-Aid for Scientific Research, Japan Society of Promotion of Science (grant no.17H02913).

Author contributions

R.-M.M. conceived and supervised the project. H.-Z.C. and Z.-K.S. designed the device. Z.-K.S. fabricated the devices. S.W, X.-R.M., Z.-Q.Y., Z.-K.S. and R.-M.M. performed optical characterization. H.-Z.C. and S.-L.W. carried out simulations. H.-Z.C., X.-X.W., X.H. and R.-M.M. carried out theoretical analyses. R.-M.M., Z.-K.S., H.-Z.C. and X.H. wrote the manuscript. All authors fully contributed to the project.

Competing interests

The authors declare no competing interests.

Additional information

Supplementary information is available for this paper at https://doi.org/10.1038/s41565-019-0584-x.

Correspondence and requests for materials should be addressed to R.-M.M.

Peer review information *Nature Nanotechnology* thanks Alexander Khanikaev and the other, anonymous, reviewer(s) for their contribution to the peer review of this work.

nature research

Corresponding author(s): *Double-blind peer review submissions: write DBPR and your manuscript number here instead of author names.*

Lasing Reporting Summary

Nature Research wishes to improve the reproducibility of the work that we publish. This form is intended for publication with all accepted papers reporting claims of lasing and provides structure for consistency and transparency in reporting. Some list items might not apply to an individual manuscript, but all fields must be completed for clarity.

For further information on Nature Research policies, including our data availability policy, see Authors & Referees.

Experimental design

Please check: are the following details reported in the manuscript?

1. Threshold

Plots of device output power versus pump power over a wide range of values indicating a clear threshold	☒ Yes ☐ No	ig.3b in the main text shows the light-light curve in linear and log scales of a typical device indicating a clear threshold for lasing process.

2. Linewidth narrowing

Plots of spectral power density for the emission at pump powers below, around, and above the lasing threshold, indicating a clear linewidth narrowing at threshold	☒ Yes ☐ No	ig.3a show the spectrum of the device under different pump powers, which indicate a clear linewidth narrowing of the emission. Below threshold, the linewidth of the spontaneous emission is ~100 nm. Above threshold, the lasing linewidth is ~0.25 nm (Supplementary Fig. 11).
Resolution of the spectrometer used to make spectral measurements	☒ Yes ☐ No	The resolution of our spectrometer is ~0.1 nm.

3. Coherent emission

Measurements of the coherence and/or polarization of the emission	☒ Yes ☐ No	We have measured the first order of coherence which matches well with our simulated results (Fig. 3c and e, Fig. 4b, Supplementary Fig. 11). The polarization of the emission is shown in Fig. S13.

4. Beam spatial profile

Image and/or measurement of the spatial shape and profile of the emission, showing a well-defined beam above threshold	☒ Yes ☐ No	The spatial profile of the emission has been imaged, and it indicates the existence of a well-defined beam above threshold as shown in Fig.3e and 3f.

5. Operating conditions

Description of the laser and pumping conditions *Continuous-wave, pulsed, temperature of operation*	☒ Yes ☐ No	Methods section and Abstract
Threshold values provided as density values (e.g. W cm^{-2} or J cm^{-2}) taking into account the area of the device	☒ Yes ☐ No	Main text. The threshold values are provided as a density value (kW cm^-2) taking into the account the area of the pump laser spot.

6. Alternative explanations

Reasoning as to why alternative explanations have been ruled out as responsible for the emission characteristics *e.g. amplified spontaneous, directional scattering; modification of fluorescence spectrum by the cavity*	☒ Yes ☐ No	We have ruled out alternative explanations.

7. Theoretical analysis

Theoretical analysis that ensures that the experimental values measured are realistic and reasonable *e.g. laser threshold, linewidth, cavity gain-loss, efficiency*	☒ Yes ☐ No	We have calculated mode profiles of the lasing modes, which matches with the experimental ones (Fig.2e and 3f). These simulations ensure that the experimental values measured for characteristics are realistic and reasonable

8. Statistics

Number of devices fabricated and tested	☒ Yes ☐ No	Over 40 devices have been fabricated and tested.
Statistical analysis of the device performance and lifetime (time to failure)	☒ Yes ☐ No	All of them lase stably at room temperature over the tested months.